HHS Public Access

Author manuscript

Med Phys. Author manuscript; available in PMC 2025 May 18.

Published in final edited form as:

Med Phys. 2024 July ; 51(7): 5081–5093. doi:10.1002/mp.17050.

Secondary neutron dosimetry for conformal FLASH proton therapy

Dixin Chen[1], **Seyyedeh Azar Oliaei Motlagh**[1], **François Vander Stappen**[2], **Rudi Labarbe**[2], **Beryl Bell**[2], **Michele Kim**[1], **Boon-Keng Kevin Teo**[1], **Lei Dong**[1], **Wei Zou**[1], **Eric Stanton Diffenderfer**[1]

[1]Department of Radiation Oncology, University of Pennsylvania, Philadelphia, Pennsylvania, USA

[2]Ion Beam Applications S.A. (IBA), Louvain-la-Neuve, Belgium

Abstract

Background: Cyclotron-based proton therapy systems utilize the highest proton energies to achieve an ultra-high dose rate (UHDR) for FLASH radiotherapy. The deep-penetrating range associated with this high energy can be modulated by inserting a uniform plate of proton-stopping material,known as a range shifter, in the beam path at the nozzle to bring the Bragg peak within the target while ensuring high proton transport efficiency for UHDR. Aluminum has been recently proposed as a range shifter material mainly due to its high compactness and its mechanical properties. A possible drawback lies in the fact that aluminum has a larger cross-section of producing secondary neutrons compared to conventional plastic range shifters. Accordingly, an increase in secondary neutron contamination was expected during the delivery of range-modulated FLASH proton therapy, potentially heightening neutron-induced carcinogenic risks to the patient.

Purpose: We conducted neutron dosimetry using simulations and measurements to evaluate excess dose due to neutron exposure during UHDR proton irradiation with aluminum range shifters compared to plastic range shifters.

Methods: Monte Carlo simulations in TOPAS were performed to investigate the secondary neutron production characteristics with aluminum range shifter during 225 MeV single-spot proton irradiation. The computational results were validated against measurements with a pair of ionization chambers in an out-of-field region (≤ 30 cm) and with a Proton Recoil Scintillator-Los Alamos rem meter in a far-out-of-field region (0.5–2.5 m). The assessments were repeated with solid water slabs as a surrogate for the conventional range shifter material to evaluate the impact of aluminum on neutron yield. The results were compared with the International Electrotechnical Commission (IEC) standards to evaluate the clinical acceptance of the secondary neutron yield.

Correspondence: Eric Stanton Diffenderfer, Department of Radiation Oncology, University of Pennsylvania, 3400 Civic Center Blvd., PCAM 2 West, Philadelphia, PA 19104, USA. Eric.Diffenderfer@pennmedicine.upenn.edu.
Present address: Dixin Chen,Department of Radiation Oncology, Stanford University, Stanford, California 94025, USA, Beryl Bell,Department of Physics, Drexel University, Philadelphia, Pennsylvania 19104, USA

CONFLICT OF INTEREST STATEMENT

François Vander Stappen, Rudi Labarbe, and Beryl Bell are employees at IBA.

SUPPORTING INFORMATION

Additional supporting information can be found online in the Supporting Information section at the end of this article.

Results: For a range modulation up to 26 cm in water, the maximum simulated and measured values of out-of-field secondary neutron dose equivalent per therapeutic dose with aluminum range shifter were found to be (0.57 ± 0.02) mSv/Gy and (0.46 ± 0.04) mSv/Gy, respectively, overall higher than the solid water cases (simulation: (0.332 ± 0.003) mSv/Gy; measurement: (0.33 ± 0.03) mSv/Gy). The maximum far out-of-field secondary neutron dose equivalent was found to be (8.8 ± 0.5) μSv⁄Gy and (1.62 ± 0.02) μSv⁄Gy for the simulations and rem meter measurements, respectively, also higher than the solid water counterparts (simulation: (3.3 ± 0.3) μSv⁄Gy; measurement: (0.63 ± 0.03) μSv⁄Gy).

Conclusions: We conducted simulations and measurements of secondary neutron production under proton irradiation at FLASH energy with range shifters. We found that the secondary neutron yield increased when using aluminum range shifters compared to conventional materials while remaining well below the non-primary radiation limit constrained by the IEC regulations.

Keywords

FLASH; proton therapy; secondary neutron

1 | INTRODUCTION

Proton therapy has gained increasing interest in past decades as it offers superior dose conformity and reduces the adverse effects on healthy tissues compared to photon radiotherapy.[1] The use of proton therapy has been shown to reduce the incidence of secondary cancers in long-term survivors, making it a more favorable option especially for pediatric patients and patients with localized tumors.[2–5] Since 2014, the concept of FLASH therapy has emerged as a promising approach to greatly reduce the toxicity in radiotherapy treatments by delivering an ultra-high dose rate (UHDR) of radiation exceeding 40 Gy/s.[6,7] Early preclinical studies and machine developments have demonstrated the feasibility of UHDR FLASH proton therapy that harnesses the tissue sparing from proton beam characteristics and FLASH effects.[8–11]

Despite its potential benefits, FLASH proton therapy presents additional challenges in the course of its development. The highest proton energies at around 225 MeV need to be used for a cyclotron-based proton therapy in order to maintain high particle transport efficiency for a UHDR. The range associated with 225 MeV protons is around 32 cm in water, which exceeds the typical depth of the lesions in a patient. In our institute, conventional proton therapy involves an upstream range modulator and sometimes a range shifter – a uniform slab made of polymethyl methacrylate (PMMA) – in the snout to bring the proton range closer to the surface. In the case of cyclotron-based FLASH proton therapy, a substantial thickness of PMMA would be needed to modulate the large range attributed to the maximum proton energy. As such, it has been proposed to employ an aluminum-based range shifter primarily due to its higher proton stopping power. However, when protons impinge on the range shifter, they produce secondary particles, notably secondary neutrons, which possess a greater biological effectiveness compared to photons and electrons. This heightened biological impact may cause damage to healthy tissues, potentially leading to a second cancer in patients.[12–14] Aluminum, as a high-Z material relative to plastic, possesses a higher cross-section in producing secondary neutrons under proton irradiation. Therefore,

it is necessary to evaluate the level of secondary neutrons when using an aluminum range shifter to ensure that the secondary neutrons produced during UHDR irradiation are within clinically acceptable limits.

There exist various dosimetry quantities that can be utilized for the evaluation of secondary neutrons in clinical settings. Among these quantities, the AAPM Task Group 158 has recommended using the ambient neutron dose equivalent as the measure to assess the neutron contamination during proton therapy.[15] Common neutron dosimetry methods include directly measuring the neutron dose equivalent using neutron detectors such as Bonner sphere systems[16–21] or REM counters,[22–27] and performing Monte Carlo (MC) simulations, which would require further verification and bench-marking with measurement results.[28–32] Previous studies on secondary neutron dosimetry using either measurements or simulations or both have shown that neutron contamination during proton therapy remains at a low level.[33–37] Nevertheless,studies on secondary neutron dose contamination in UHDR radiotherapy have remained scarce. A recent shielding study suggested that the rise of secondary neutrons from the use of FLASH proton beam challenges the conventional shielding design.[38] It is thus crucial to ensure a safe clinical translation of the FLASH technique while minimizing the neutron-induced carcinogenic risk posed to patients.

To discuss secondary neutron characteristics, it is convenient to classify neutrons according to their kinetic energies: thermal, intermediate, fast, and relativistic neutrons. Thermal neutrons exhibit thermal equilibrium with matter and have a neutron cross-section inversely proportional to their velocities. Following a Maxwell–Boltzmann distribution, their velocities are most probable to be found at 2.2 km/s at 295 K, corresponding to an energy of 0.025 eV.[39] Intermediate neutrons have energy ranging from 0.5 eV to 100 keV. Fast neutrons have energies ranging from slightly lower than 100 keV to 20 MeV, where elastic scattering between neutrons and matter is one of the most important interactions for these neutrons. Relativistic neutrons are the ones having energy greater than 20 MeV. For these high-energy neutrons, inelastic scattering becomes more important than elastic scattering especially when they interact with high-Z materials.

In this paper, we present secondary neutron measurements and simulation results for range-modulated proton irradiation at FLASH energy. We describe how neutron dosimetry was performed during 225-MeV proton irradiation with aluminum and solid water range shifters. We also compare our findings to regulatory standards and previous shielding surveys on secondary neutrons for proton therapy. Overall, this study improves our understanding of the risks associated with neutron exposure during UHDR proton radiotherapy and provides an experimentally validated computational approach for investigations in the shielding design of future FLASH proton therapy facilities that could ideally minimize unwanted secondary neutron doses to patients.

2 | METHODS AND MATERIALS

To evaluate the secondary neutron dose due to the use of a range shifter in FLASH proton therapy, we performed experimental measurements of the neutron production during range-modulated 225-MeV proton irradiation from an IBA Proteus Plus proton system. In parallel,

we simulated the secondary neutron production in a GEANT4-based MC tool TOPAS (version 3.9).[40] Figure 1 shows a beam snout designed for the range-modulated FLASH proton pencil beam scanning and a gold-anodized aluminum range shifting plate used in the experiments. The snout featured a plastic ridge filter for modulating the beam with a spread-out Bragg peak (SOBP) and incorporated five aluminum range-shifting plates, each with a thickness of 1.5 cm, alongside a brass aperture for beam collimation. Note that the ridge filter was not included in our experiments since our field consisted of a single pencil beam spot and an aperture was present only in the simulations with the beam passing through its center.

Table 1 shows a total of four tested groups providing a range modulation from 6.6 to 25.8 cm. The length of range modulation was obtained empirically by comparing the depth of the Bragg peak of each configuration through MC simulations. The aluminum range shifter material proposed for FLASH proton therapy was tested in both simulations and measurements. In addition, range shifters made of Solid Water (Model number 457, Gammex/RMI, Wisconsin, USA), as a surrogate for the PMMA range shifter material used in conventional proton therapy, were tested to investigate the effect on secondary neutrons from different range shifting materials.

2.1 | Methods of measurements

The secondary neutron yield was measured using a pre-manufactured pair of ionization chambers and a Model 2241-3 Proton Recoil Scintillator-Los Alamos (PRESCILA) neutron rem meter (LUDLUM Measurements, Inc., Sweetwater, TX, USA). In each measurement, a single-spot proton pencil beam at 225 MeV was delivered from the proton system with a gantry angle of 270°. The delivered absorbed dose in water at the Bragg peak ranged from 15.2 to 30.5 Gy across different configurations. We employed a conventional dose rate, considering that the neutron dose is a cumulative dose over time and a lower dose rate allows the accurate dose response on the measuring devices.

2.1.1 | Dual-ionization chamber method: The absorbed dose from secondary neutrons in water was measured at three positions (A1,A2,and A3). These three points were also used to validate the simulation results. The dose was measured by a pair of pre-manufactured ionization chambers (shown in Figure 2a) which are capable of separating neutron dose from a mixed background field of neutrons, photons, and protons.[44,45] The paired chamber technique,also known as the dual-ionization chamber method, relies on the different responses of the two chambers to the impinging neutrons. For our chambers, one is made of a tissue-equivalent wall filled with tissue-equivalent gas (TE-TE); the other one is composed of a magnesium wall and argon gas (Mg-Ar). The two chambers have similar sensitivities to protons and photons but with distinct sensitivities to neutrons. The TE-TE chamber is more sensitive to the change in the number of neutrons in the mixed field due to the hydrogenous property of the TE material. The Mg-Ar chamber is made of non-hydrogenous and high-Z materials and thus gives a lower cross-section of neutron interaction, resulting in a lower sensitivity in detecting neutrons. The two chambers are of the same geometry dimensions with a 9.14 cm^3 active volume and an inner diameter of 19.05 mm. For each chamber, the thickness of the cathode wall is 3.18 mm and the diameter

of the anode is 6.35 mm. The dose-to-water calibration factor is 3.44×10^6 Gy/C and 2.33×10^6 Gy/C for the TE-TE chamber and the Mg-Ar chamber respectively. The chamber readings can be related to the neutron dose D_N and the proton and photon dose $D_{p+\gamma}$ as

$$k_{\text{TE-TE}} \cdot D_N + D_{p+\gamma} = R_{\text{TE-TE}} \quad (1)$$

$$k_{\text{Mg-Ar}} \cdot D_N + D_{p+\gamma} = R_{\text{Mg-Ar}}, \quad (2)$$

where $R_{\text{TE-TE}}$ and $R_{\text{Mg-Ar}}$ represent the readings of the TE-TE and Mg-Ar chambers, and $k_{\text{TE-TE}}$ and $k_{\text{Mg-Ar}}$ correspond to the relative neutron sensitivities of the two chambers, which are functions of incident neutron energy.

The neutron response functions of the two chambers were obtained in the MC simulations. For the TE-TE chamber, the tissue-equivalent wall material was modeled as A150 TE plastic, and the gas was composed of methane-based tissue-equivalent gas. Each chamber had the same dimension as the physical ones as specified in the previous work and was immersed in the center of a $(30 \times 30 \times 30)$ cm^3 water phantom.[45] A neutron beam source was placed 5 cm outside the water phantom, emitting 5×10^6 monoenergetic neutrons that incident perpendicularly to the cylindrical axis of the chamber with the entire chamber covered. The total absorbed dose in the gas volume was scored as a function of incident neutron energy ranging from 1 MeV to 230 MeV. To convert the absorbed dose-to-gas to dose-to-water,we further modeled the chamber with the same dimensions but composed of water of areal densities equivalent to the areal densities of the original materials. We repeated the simulation with a reference 6-MV photon beam to obtain the relative neutron sensitivity k_i at a specific neutron energy as following

$$k_i = \frac{d_i^{\text{neutron}} / d_{\text{water}_i}^{\text{neutron}}}{d_i^{\text{photon}} / d_{\text{water}_i}^{\text{photon}}},$$

where i represents the TE-TE or Mg-Ar chamber, d_i^{neutron} and d_i^{photon} are the absorbed dose deposited in the gas from neutron and photon irradiation respectively, $d_{\text{water}_i}^{\text{neutron}}$ and $d_{\text{water}_i}^{\text{photon}}$ are the absorbed dose deposited in the water with equivalent areal density from neutron and photon irradiation respectively. Figure 3 showed the neutron sensitivity of the two chambers as a function of neutron energy (details in Figure S1). For the neutrons with energies below 1 MeV, the sensitivities of the same pair of ion chambers reported in a previous study were adopted.[45] This leads to relative neutron sensitivities of 1.0 and 0.1 being applied for neutrons below 1 MeV in the TE-TE and the Mg-Ar chamber respectively. The proton and photon sensitivity was assumed to be 1 for both chambers. The physical dose measured by the ion chambers was converted to dose equivalent using radiation weighting factors computed using a group of continuous functions of neutron energy recommended in ICRP

103.[14] A fluence-weighted average of the weighting factor at each point was then calculated using the simulated neutron energy fluence at each point of measurement.

Figure 2b shows the dual-ionization chamber measurement setup where the two chambers were attached to a three-dimensional scanning platform in a Blue Phantom (IBA, Louvain-La-Neuve, Belgium), which is a (675 × 645 × 560) mm^3 water tank. The chamber was mounted onto the scanning stage with a 3D-printed dual chamber holder. The proton beam impinged orthogonally to the water tank through a set of range shifters. Additional range shifter plates were added at the upstream edge of the existing range shifters. The downstream edge of the range shifters was placed at 14.15 cm from the surface of the water tank. This air gap between the range shifter and the water tank was determined by the sum of the length of a 6-cm thick cylindrical brass aperture (not present), a 5-cm air gap downstream from the aperture, and a 3.15-cm air gap downstream from the range shifter. The two ion chambers were placed symmetrically at 0, 5, or 10 cm laterally from the beam axis and 5 cm downstream from the Bragg peak in the water tank shown in Figure 2c.

2.1.2 | PRESCILA rem meter measurements: Far out-of-field secondary neutron during 225-MeV proton irradiation with range modulation was measured using a PRESCILA rem meter shown in Figure 4. This scintillator-based detector is capable of neutron detection at high sensitivity with a wider range of energy response compared to conventional moderator-based rem meters.[46] Figure 4b shows the measurement setup with the detector aligned along a horizontal axis 0.3 m downstream from the range shifter. We measured the neutron dose equivalent by placing the rem meter at a distance of 0.5, 1,and 2 m from the central axis,denoted as the points B1, B2, and B3. Similar to the dual ion chamber setup, aluminum plates or solid water slabs were added upstream from the range shifter. The proton beam was delivered for an extended amount of time for the PRESCILA readout to be stabilized. We recorded the neutron dose rate in units of rem/h over 30 s of delivery using a monitoring camera inside the treatment room and then computed the integrated dose equivalent.

2.2 | Monte Carlo simulations

A total of six physics modules were included in the simulations. “G4em-standard_opt4”was used for electromagnetic interactions. “g4h-phy_QGSP_BIC_HP” was used for inelastic nuclear interactions with a high precision neutron model. The decay of all long-lived hadrons and leptons was managed by “g4decay”. Default physics modules “g4ion-binarycascade”, “g4h-elastic_HP”, and “g4stopping”were also included for inelastic interactions and other particle simulations.

Figure 5 shows a schematic of the MC simulation setup with positions A1, A2, and A3 used for measurement validation as described in Section 2.1. No room details or walls were implemented in the simulations. A single Gaussian proton beam of energy (225.0 ± 0.6) MeV and a spot size with a full width at half maximum of (1 × 1) cm^2 was simulated in the air and impinged onto a range shifter of surface area (10 × 10) cm^2. Table 2 shows the composition of each range shifter material used in the MC simulations. A cylindrical brass aperture with a square opening of (7 × 7) cm^2 was placed after a 3.15-cm air gap

downstream from the range shifter. The outer radius and the thickness of the aperture were 10.7 cm and 6 cm respectively. A water phantom of volume (30 × 30 × 40) cm^3 was placed after a 5-cm air gap downstream from the aperture. The thickness of the range shifter was increased at the upstream end in order to keep a fixed distance between the range shifter and the water surface. The isocenter was defined on the beam axis at the Bragg peak depth in water. The beam source was placed at a fixed distance of 50 cm from the isocenter.

Several dosimetric quantities were obtained in the water phantom, including neutron fluence (ϕ_N), absorbed dose from all particles and neutrons only, and ambient neutron dose equivalent $H^*(10)$.[14] (5×10^6) histories were simulated 4 times for each setup to obtain a mean value with a standard deviation for each quantity. The neutron fluence was scored per unit area and logarithmically binned into 140 energy bins from 10^{-10} MeV to 10^3 MeV. It is worth noting that the quantity fluence typically refers to the number of particles crossing per unit cross-sectional area. In TOPAS, fluence is calculated differently: it is obtained by dividing the total distance traveled by particles passing through the material by the volume of the irradiated material. The neutron fluence was normalized by unit therapeutic dose (D) defined as the total absorbed dose at the Bragg peak. The normalized fluence was reported in units of lethargy (u), a logarithmic measure of neutron energy that describes the relative decrease in neutron speed.[41] This unit is convenient for grouping neutrons with similar energies. The ambient neutron dose equivalent was obtained by multiplying the incident neutron fluence with linearly-interpolated fluence to ambient dose equivalent conversion coefficients across the neutron energy spectrum.[42] Similar to the neutron fluence, the neutron absorbed dose and the ambient neutron dose equivalent were also normalized by unit therapeutic dose. Moreover, a particle origin filter was applied to score the quantities of particles produced in different components, namely the range shifter and the water phantom. To compare the change in dose and dose equivalent among different setups, we computed their percentage difference with standard error propagation on their corresponding uncertainties.

While secondary neutron simulations near the irradiation field offer insights into excess neutron doses in the vicinity of or within the patient's body, the far out-of-field neutron dose holds arguably greater clinical relevance. With this consideration, we conducted simulations of secondary neutrons in the far out-of-field region with no water tank present in the beam line. Figure 6 shows the simulation setup measuring neutrons in the air at a lateral distance of 0.5 to 2 m from the isocenter, located 0.3 m from the range shifter. The scoring region was a rectangular prism of volume (1 × 1 × 200) cm^3, binned into 200 voxels of 1 cm^3 along the x-axis. Three points (B1, B2, B3) were selected in the scoring volume for measurement validation. Neutron fluence, total absorbed dose, and ambient neutron dose equivalent were scored in each voxel.

Furthermore, the ambient neutron dose equivalent was compared with the out-of-field secondary neutron radiation standard provided by the International Electrotechnical Commission (IEC).[43] The standard specifies that the absorbed dose from neutrons at 1.5–2 m should be lower than 0.08% of the dose at the isocenter within a maximum 60-mm range modulation. In other words, under this range modulation condition, the maximum neutron dose allowed is recommended to be 0.8 mGy per 1 Gy of the therapeutic dose. This neutron

dose threshold can be converted to dose equivalent per therapeutic dose by employing the weighting factor due to neutron radiation. Group A setup was used for the comparison,as the corresponding range shifters provide the closest range modulation of approximately 66 mm. A minimum fluence-weighted average for the weighting factor was found to be 5 and was used to calculate the lowest and hence the most strict threshold value.[14] The absorbed neutron dose limit was converted to a dose equivalent limit of 0.8 mGy/Gy × 5 = 4 mSv/Gy. In practice, the allowed neutron dose equivalent is expected to be higher due to the wide range of possible neutron energies resulting in a higher weighting factor.

3 | RESULTS

3.1 | Simulation validation with measurement

Figure 7 showed the simulated and measured secondary neutron dose equivalent per therapeutic dose at three points of measurement A1,A2,and A3 in the water phantom with aluminum or solid water range shifters of a water equivalent thickness of 6.6, 13.0, 19.4, and 25.8 cm corresponding to Group A, B, C, and D. Both simulations and measurements showed a decrease in secondary neutrons when the points went further from the central axis. We found a general increase between 18% to 52% in the secondary neutron dose equivalent for the aluminum cases compared to the solid water cases at all three points in both simulations and measurements. The greatest simulated neutron dose equivalent was observed at (0.57 ± 0.02) mSv/Gy at A1 in Group D using aluminum range shifters, where the aluminum plates reached a thickness of 12 cm. In comparison, with the same water equivalent thickness, the 25.9-cm solid water slabs resulted in a maximum neutron dose equivalent of (0.332 ± 0.003) mSv/Gy in TOPAS and (0.33 ± 0.03) mSv/Gy using ion chambers. In this particular case, the aluminum range shifter yielded a secondary neutron dose equivalent 1.7 times greater than that of solid water for the same amount of range modulation. As the thickness of the range shifter decreased, the amount of secondary neutron dose equivalent decreased for the aluminum case,while no major change was found for the solid water case, especially for A1 and A3.

Figure 8 shows the simulated and measured far out-of-field secondary neutron dose equivalent per therapeutic dose at a distance within 2.5 m laterally from the central axis with both aluminum and solid water range modulation. One can observe a consistent trend in both the simulation and measurement results across all experimental groups. As the thickness of the range shifter increased, there was a corresponding increase in secondary neutron yield for both aluminum and solid water configurations. Following the inverse square law, the neutron dose equivalent decreased with increasing distance from the beam axis. The most prominent increase in secondary neutron yield was observed in Group D, where the range shifters were the thickest. In this group, the simulated neutron dose equivalent per therapeutic dose for the aluminum case reached (8.8 ± 0.5) μSv/Gy at 1 m from the beam axis,which was 2.7 times greater than the solid water counterpart. The measured values exhibited a similar increase, with the aluminum case yielding 2.6 times greater dose equivalent compared to solid water. From 1.5 to 2 m in Group A, both the simulated and measured values of neutron dose equivalent fell below the dose equivalent limit of 4 mSv/Gy mentioned in Section 2.2 and were thus in agreement with the IEC

standard. It is worth noting that the measured dose equivalent was overall lower than the simulated value for all the cases. The discrepancies between simulation and measurement results became less pronounced in the other three groups as range modulation decreased with Group A displaying the closest agreement between the two.

Table 3 shows a summary of the simulated and measured secondary neutron dose equivalent per therapeutic dose. Within close proximity to the irradiation field − 5 cm downstream from the beam port and within ≤15 cm laterally from the central axis – the increase in the simulated dose equivalent spanned from (22 ± 5)% to (96 ± 8)% for aluminum range shifters compared to solid water. At a further distance of 1–2 m from the central axis, the simulated secondary neutron dose equivalent for the aluminum case exhibited an average two-fold increase compared to the solid water case. The measured values generally aligned with the simulation results, validating the influence of range modulation material and points of measurement on secondary neutron dose equivalent values. The simulated values of dose equivalent were on average within 10.7% difference from the measurement values, with the largest difference of 32.4% at A3 for Group A aluminum and the smallest difference of 1.4% at A1 for the same group of aluminum.

3.2 | Simulated secondary neutron production characteristics

Figure 9 shows the simulated ambient neutron dose equivalent distribution per therapeutic dose in the *xz*-plane for Groups A and C. The maximum dose equivalent was 19.9 mSv/Gy for Group A with an aluminum range shifter at a depth of 4.2 cm from the water surface, which was greater than a maximum value of 15.8 mSv/Gy at a depth of 5.4 cm for solid water in the same group. In Group C, the maximum values of the dose equivalent per therapeutic dose were found at a depth of 3.0 cm for both aluminum and solid water with a value of 17.2 and 12.1 mSv/Gy respectively. The neutron dose equivalent decreased quickly to less than approximately 5 mSv/Gy after the Bragg peak in all the configurations.

The ambient neutron dose equivalent per therapeutic dose profiles along the central and lateral axes for Group C are shown in Figure 10. We also separated the secondary neutrons that originated in the range shifter before traveling downstream from the neutron produced solely in the water tank. A dose equivalent build-up region was found due to the secondary neutrons produced in the water phantom near the surface of the water phantom before decreasing exponentially as neutrons traveled downstream in the water phantom. Accordingly, when we only considered secondary neutrons produced in the range shifter, no build-up region was found near the water surface (Figure 10c). Along the lateral axis, the dose equivalent dropped from a maximum value at slightly over 6 mSv/Gy following the inverse square law as neutrons laterally scattered across the water phantom.

Figure 11 shows the secondary neutron fluence of Groups A and C in lethargic unit per therapeutic dose at 5 cm beyond the Bragg peak along the central axis as a function of neutron energy. The neutron fluence was distributed as a continuous spectrum with one peak at the thermal region and two peaks overlapping in the fast and relativistic regions. In both groups, the aluminum neutron fluence at the thermal and relativistic peaks increased by a factor of 1.5 and 1.4 respectively compared to the solid water.To further investigate the impact of implementing the range shifters, the fluence spectra were separated into two

components by the origin of secondary neutrons. This allows the neutrons produced in the range shifter to be isolated from total neutrons, which primarily consist of neutrons produced in the water phantom. From the component spectra, we can see that the fluence in the thermal region was dominated by the neutrons produced in the water phantom. Comparing Groups A and C, the increase in the thickness of the range shifters resulted in a higher production of secondary neutrons in the relativistic energy region on the spectra of neutrons produced in the range shifter, with the relativistic peak increased by a factor of 3.9 when the thickness of aluminum changed from 3 cm to 9 cm. In comparison, the relativistic peak increased by a factor of 2.6 when the thickness of solid water changed from 6.4 to 19.5 cm, providing the same amount of range modulation in water as the aluminum.

4 | DISCUSSION

The results from measurements and MC simulations demonstrated an increase in the secondary neutron fluence when replacing conventional plastic range shifters with aluminum for the UHDR proton beam. This is expected since the cross-section of the interaction between protons and nuclei in the range shifter material increases when there are a higher number of atoms present in the range shifter. Additionally, due to the hydrogenous property of the plastic range shifter, the secondary neutrons produced in it may be readily absorbed before traveling downstream to the water phantom. While the neutron dose produced with the aluminum range shifter was higher, it remained well below the IEC threshold. Taking into account the superior physical and mechanical properties of aluminum compared to solid water, the results suggested aluminum range shifters as an acceptable alternative for range-modulated FLASH proton therapy.

On the neutron fluence spectra, the presence of a thermal peak resulted from fast neutrons slowing down when scattering in the water phantom. The simulation results showed that the neutrons at the relativistic energy peak primarily originated from the range shifter. The peak in the relativistic region extends to the fast neutron region, suggesting the production of fast neutrons from evaporation processes between the secondary photons and the nucleons in the matter. The relativistic peak can also be found in other photon or particle therapies with energy higher than the neutron binding energy at approximately 7 MeV in large atomic number materials present in the beam path inside the treatment room. The neutron dose equivalent in the water tank measured using dual-ion chambers was found to be on the same order of magnitude compared to the simulated counterparts. However, the measured values are lower than the simulated ones at all positions for most cases, suggesting a potential overestimation in the simulations. One possible reason may be the positioning of the ion chambers in the water tank. One can see from the dose map in Figure 9, the dose equivalent in the region beyond the Bragg peak falls off quickly. Hence, a slight mispositioning may result in a large change in the value of the dose equivalent.

4.1 | Limitations in the simulations

Our study presents several discrepancies in the setups when compared to the actual FLASH proton delivery setups. Firstly, a single spot beam was used in our simulations and measurements, while FLASH proton irradiation is likely to use a dose map with SOBP

beams modulated by a ridge filter upstream in the nozzle. This may result in a higher neutron yield due to the increase in the proton dose. Clinical treatment plans that position the pencil beam near the aperture may also result in an increased production of secondary neutrons. Vedelago et al. reported a difference in neutron fluence between pristine and SOBP beams. Specifically, they found the ratio between the neutron fluence in the fast and relativistic region and the thermal region was higher than the ratio for pristine peaks due to the increase in the number of impinging protons.[47] The MC beam source was placed at a closer distance from the isocenter compared to the typical virtual source distance during the actual delivery of the proton beam, resulting in a possible overestimation of neutron dose in the water phantom. In addition, the presence of the ridge filter and the aperture in the snout could potentially introduce more thermal neutrons in the water phantom leading to a higher out-of-field neutron dose.

Secondly, there was no room component such as walls or couch simulated. The lack of room geometry was expected to result in an underestimation in the simulated far out-of-field dose equivalent since we have fewer room-return thermal neutrons. Englbrecht et al. compared no-room MC simulation to the ones with full-room geometry simulated by Trinkl et al. and found mismatches in the secondary neutron fluence spectra at 2 m from the isocenter.[20,48] These studies showed non-negligible neutron contributions from the room components, namely outer walls and concrete floor, peaked in both the thermal region and fast region with 200-MeV protons as the primary beam. In our study, however, we found an overestimation in the simulated neutron dose compared to the measurements. This overestimation may thus be primarily due to the low detection efficiency during the measurements, which outweighed the underestimation due to the lack of room geometry. More comprehensive simulations with full-room components are needed to obtain a more accurate neutron dose estimation at positions far from the irradiating field.

Another discrepancy exists in regard to the delivery system and method for FLASH proton therapy. The neutron contamination may vary depending on the proton delivery systems. There are currently three major FLASH proton delivery methods:double scattering,pencil beam scanning, and hybrid system.[49–51] Several studies compared different delivery methods in conventional proton therapy and reported that double scattering tends to give a higher secondary neutron dose compared to pencil beam scanning primarily due to the components such as scatterers and apertures present in the nozzle for the double scattering method.[33,37,52] However, the pencil beam scanning system for FLASH delivery also requires extra components in the snout to create SOBP plans and achieve range modulation. This study provides confidence in using MC simulations to estimate excess neutron dose with more clinical-related fields beyond a single-spot beam. Further investigations with larger fields are needed to ensure that no extra shielding for excess neutrons would be required for FLASH delivery.

5 | CONCLUSIONS

In this study, we conducted secondary neutron dosimetry during proton irradiation with range shifters at a FLASH irradiation energy to investigate the effect of range modulation using aluminum on the production of secondary neutrons. We performed measurements

and MC simulations in TOPAS to obtain out-of-field secondary neutron yield with a single-spot proton beam. The simulation results were validated by the measurements using a pair of ionization chambers at three positions and a PRESCILA rem meter at three further locations. The aluminum range shifter was found to produce an increased number of secondary neutrons compared to the solid water range shifter. In the far-out-of-field region, the secondary neutron dose equivalents per therapeutic dose on the order of unity in units of μSv/Gy for the aluminum cases, all below the maximum allowed non-primary radiation level according to the IEC standards. The simulated neutron fluence spectrum was found to be predominantly characterized by thermal, fast, and relativistic neutrons, with the increase in neutron fluence primarily occurring in the relativistic neutron energy range. The experimental validation of the simulation sets the foundation for future investigations from a computational-only approach, allowing confident estimation of excess neutron dose levels with larger field sizes for more clinically pertinent configurations. These investigations would be needed for further determination of the adequacy of the current shielding design for the safety of the patient and medical personnel involved in the treatment. Overall, the simulations validated through measurements at a wide range of distances provided confidence in using computational methods for a conservative evaluation of secondary neutrons in range-modulated FLASH proton irradiation.

Supplementary Material

Refer to Web version on PubMed Central for supplementary material.

ACKNOWLEDGMENTS

This work was supported by Ion Beam Applications (IBA) Proton Therapy and National Institutes of Health (NIH) grant P01CA257904.

Funding information

IBA Proton Therapy; National Institutes of Health, Grant/Award Number: P01CA257904

DATA AVAILABILITY STATEMENT

The data supporting the findings of this study are available from the corresponding author on request.

REFERENCES

1. Paganetti H Proton Therapy Physics. CRC press; 2018.
2. Gallagher KJ, Taddei PJ. Analytical model to estimate equivalent dose from internal neutrons in proton therapy of children with intracranial tumors. Prot Dosimetry. 2019;183:460–468.
3. Indelicato DJ, Bates JE, Mailhot VRB, et al. Second tumor risk in children treated with proton therapy. Pediatr Blood Cancer. 2021;68:e28941. [PubMed: 33565257]
4. Romero-Expósito M, Toma-Dasu I, Dasu A. Determining out-of-field doses and second cancer risk from proton therapy in young patients – an overview. Front Oncol. 2022;12:892078. [PubMed: 35712488]
5. Mares V, Farah J, Saint-Hubert MD, et al. Neutron radiation dose measurements in a scanning proton therapy room: can parents remain near their children during treatment? Front Oncol. 2022;12:903706. [PubMed: 35912238]

6. Favaudon V, Caplier L, Monceau V, et al. Ultrahigh dose-rate FLASH irradiation increases the differential response between normal and tumor tissue in mice. Sci Transl Med. 2014;6:245ra93.
7. Harrington KJ. Ultrahigh dose-rate radiotherapy: next steps for FLASH-RT. Clin Cancer Res. 2019;25:3–5. [PubMed: 30093447]
8. Patriarca A, Fouillade C, Auger M, et al. Experimental set-up for FLASH proton irradiation of small animals using a clinical system. Int J Radiat Oncol Biol Phys. 2018;102:619–626. [PubMed: 30017793]
9. Bourhis J, Montay-Gruel P, Gonçalves Jorge P, et al. Clinical translation of FLASH radiotherapy: why and how? Radiother Oncol. 2019;139:11–17. [PubMed: 31253466]
10. Diffenderfer ES,Verginadis II,Kim MM,et al. .Design,implementation,and in vivo validation of a novel proton flash radiation therapy system. Int J Radiat Oncol Biol Phys. 2020;106:440–448. [PubMed: 31928642]
11. Darafsheh A, Hao Y, Zwart T, et al. Feasibility of proton FLASH irradiation using a synchrocyclotron for preclinical studies. Med Phys. 2020;47:4348–4355. [PubMed: 32452558]
12. ICRP. ICRP Publication 60: 1990 Recommendations of the International Commission on Radiological Protection. ICRP; 1991.
13. ICRP. ICRP Publication 92: Relative Biological Effectiveness (RBE), Quality Factor (Q), and Radiation Weighting Factor (wR). ICRP; 2003.
14. ICRP. ICRP Publication 103: 2007 Recommendations of the International Commission on Radiological Protection. ICRP; 2007.
15. Kry SF, Bednarz B, Howell RM, et al. AAPM TG 158: measurement and calculation of doses outside the treated volume from external-beam radiation therapy. Med Phys. 2017;44:e391–e429. [PubMed: 28688159]
16. Yan X, Titt U, Koehler A, Newhauser W. Measurement of neutron dose equivalent to proton therapy patients outside of the proton radiation field. Nucl Instrum. 2002;476:429–434.
17. Schneider U, Agosteo S, Pedroni E, Besserer J. Secondary neutron dose during proton therapy using spot scanning. Int J Radiat Oncol Biol Phys. 2002;53:244–251. [PubMed: 12007965]
18. Howell RM, Burgett EA. Secondary neutron spectrum from 250-MeV passively scattered proton therapy: measurement with an extended-range Bonner sphere system. Med Phys. 2014;41:092104. [PubMed: 25186404]
19. Mares V, Romero-Expósito M, Farah J, et al. A comprehensive spectrometry study of a stray neutron radiation field in scanning proton therapy. Phys Med Biol. 2016;61:4127–4140. [PubMed: 27171358]
20. Trinkl S, Mares V, Englbrecht FS, et al. Systematic out-of-field secondary neutron spectrometry and dosimetry in pencil beam scanning proton therapy. Med Phys. 2017;44:1912–1920. [PubMed: 28294362]
21. Domingo C, Lagares JI, Romero-Expósito M, et al. Peripheral organ equivalent dose estimation procedure in proton therapy. Front Oncol. 2022;12;882476. [PubMed: 35692801]
22. Yonai S, Matsufuji N, Kanai T, et al. Measurement of neutron ambient dose equivalent in passive carbon-ion and proton radiotherapies: neutron dose in passive carbon-ion and proton radiotherapies. Med Phys. 2008;35:4782–4792. [PubMed: 19070210]
23. Farah J, Mares V, Romero-Expósito M, et al. Measurement of stray radiation within a scanning proton therapy facility: EURADOS WG9 intercomparison exercise of active dosimetry systems: characterization of stray neutrons in proton therapy. Med Phys. 2015;42:2572–2584. [PubMed: 25979049]
24. Mojżeszek N, Farah J, Kłodowska M, et al. Measurement of stray neutron doses inside the treatment room from a proton pencil beam scanning system. Phys Med. 2017;34:80–84. [PubMed: 28131732]
25. Sharma DS, Patro KC, Manthala Padannayel N, et al. Ambient neutron and photon dose equivalent H*(10) around a pencil beam scanning proton therapy facility. Brit J Radiol. 2019;92:20190382. [PubMed: 31287739]
26. Charyyev S, Wang C-KC. Assessment of ambient neutron dose equivalent in spatially fractionated radiotherapy with protons using physical collimators. Radiat Prot Dosimetry. 2020;189:190–197. [PubMed: 32144416]

27. Zorloni G,Bosmans G,Brall T,et al. .Joint EURADOS WG9-WG11 rem-counter intercomparison in a Mevion S250i proton therapy facility with Hyperscan pulsed synchrocyclotron. Phys Med Biol. 2022;67:075005.
28. Chen KL, Bloch CD, Hill PM, Klein EE. Evaluation of neutron dose equivalent from the Mevion S250 proton accelerator: measurements and calculations. Phys Med Biol. 2013;58:8709. [PubMed: 24301001]
29. Zhou J, Fulvio AD, Beyer KA, et al. Angular distribution of neutron production by proton and carbon-ion therapeutic beams. Phys Med Biol. 2020;65:155002. [PubMed: 32197258]
30. Baradaran-Ghahfarokhi M, Reynoso F, Darafsheh A, et al. .A Monte Carlo based analytic model of the in-room neutron ambient dose equivalent for a Mevion gantry-mounted passively scattered proton system. J Radiol Prot. 2020:980–996. [PubMed: 32964859]
31. Wochnik A, Stolarczyk L, Ambrožová I, et al. Out-of-field doses for scanning proton radiotherapy of shallowly located paediatric tumours–a comparison of range shifter and 3D printed compensator. Phys Med Biol. 2021;66:035012. [PubMed: 33202399]
32. Leite AMM, Ronga MG, Giorgi M, et al. Secondary neutron dose contribution from pencil beam scanning, scattered and spatially fractionated proton therapy. Phys Med Biol. 2021;66:225010.
33. Xu XG, Bednarz B, Paganetti H. A review of dosimetry studies on external-beam radiation treatment with respect to second cancer induction. Phys Med Biol. 2008;53:R193–R241. [PubMed: 18540047]
34. Newhauser WD, Durante M. Assessing the risk of second malignancies after modern radiotherapy.Nat Rev Cancer.2011;11:438–448. [PubMed: 21593785]
35. Harrison R Out-of-field doses in radiotherapy: input to epidemio-logical studies and dose-risk models.Phys Med.2017;42:239–246. [PubMed: 28392312]
36. Newhauser WD, Schneider C, Wilson L, Shrestha S, Donahue W. A review of analytical models of stray radiation exposures from photon-and proton-beam radiotherapies. Radiat Prot Dosimetry. 2018;180:245–251. [PubMed: 29177488]
37. Hälg RA, Schneider U. Neutron dose and its measurement in proton therapy – current state of knowledge. Brit J Radiol. 2020;93:20190412. [PubMed: 31868525]
38. Xiao Z, Zhang Y, Speth J, Lee E, Mascia A, Lamba M. Evaluation of a conventionally shielded proton treatment room for FLASH radiotherapy. Med Phys. 2022;49:6765–6773. [PubMed: 36114793]
39. Brysk H Fusion neutron energies and spectra. Plasma Phys. 1973;15:611–617.
40. Perl J, Shin J, Schümann J, Faddegon B, Paganetti H. TOPAS: an innovative proton Monte Carlo platform for research and clinical applications. Med Phys. 2012;39:6818–6837. [PubMed: 23127075]
41. Narita M, Narita K. Average number of collisions necessary for slowing down of neutrons. J Nucl Sci Technol. 1989;26:819–825.
42. Pelliccioni M Overview of fluence-to-effective dose and fluence-to-ambient dose equivalent conversion coefficients for high energy radiation calculated using the FLUKA code. Radiat Prot Dosimetry. 2000;88:279–297.
43. IEC. Medical Electrical Equipment – Part 2–64: Particular Requirements for the Basic Safety and Essential Performance of Light Ion Beam Medical Electrical Equipment. IEC; 2014:60601-2-64.
44. Stinchcomb TG, Kuchnir FT, Skaggs LS. Comparison of the microdosimetric event-size method and the twin-chamber method of separating dose into neutron and gamma components. Phys Med Biol. 1980;25:51–64. [PubMed: 7360792]
45. Diffenderfer ES, Ainsley CG, Kirk ML, McDonough JE, Maughan RL. Comparison of secondary neutron dose in proton therapy resulting from the use of a tungsten alloy MLC or a brass collimator system: neutron dose from tungsten MLC or brass aperture. Med Phys. 2011;38:6248–6256. [PubMed: 22047390]
46. Olsher RH, Seagraves DT, Eisele SL, et al. PRESCILA: a new, lightweight neutron rem meter. Health Phys. 2004;86:603–612. [PubMed: 15167123]
47. Vedelago J,Geser FA,Muñoz ID,Stabilini A,Yukihara EG,Jäkel O. Assessment of secondary neutrons in particle therapy by Monte Carlo simulations. Phys Med Biol. 2022;67:015008.

48. Englbrecht FS, Trinkl S, Mares V, et al. A comprehensive Monte Carlo study of out-of-field secondary neutron spectra in a scanned-beam proton therapy gantry room. Z fur Med Phys. 2021;31:215–228.

49. Zhang G, Wang J, Wang Y, Peng H. Proton FLASH: passive scattering or pencil beam scanning? Phys Med Biol.2021;66:03NT01.

50. Farr J, Grilj V, Malka V, Sudharsan S, Schippers M. Ultra-high dose rate radiation production and delivery systems intended for FLASH. Med Phys. 2022;49:4875–4911. [PubMed: 35403262]

51. Gao Y,Liu R,Chang C,et al. .A potential revolution in cancer treatment: a topical review of FLASH radiotherapy. J Appl Clin Med Phys. 2022;23:e13790. [PubMed: 36168677]

52. Lee S, Lee C, Shin EH, et al. Measurement of neutron ambient dose equivalent in proton radiotherapy with line-scanning and wobbling mode treatment system. Radiat Prot Dosimetry. 2017;177:382–388. [PubMed: 28444374]

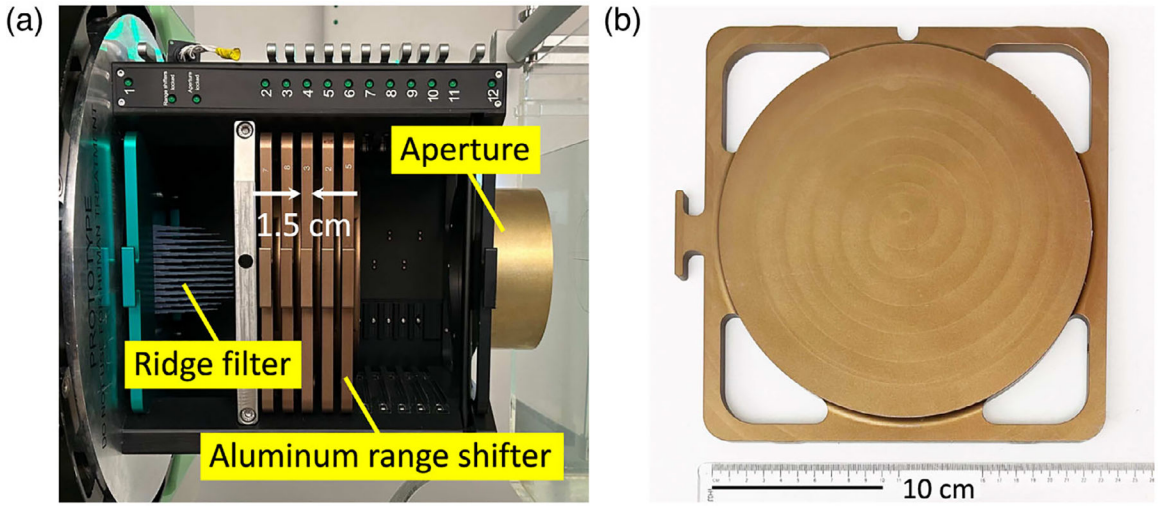

FIGURE 1.

(a) FLASH snout with a ridge filter, five aluminum range-shifting plates, and an aperture inserted. (b) Gold-anodized aluminum range shifter of thickness 1.5 cm.

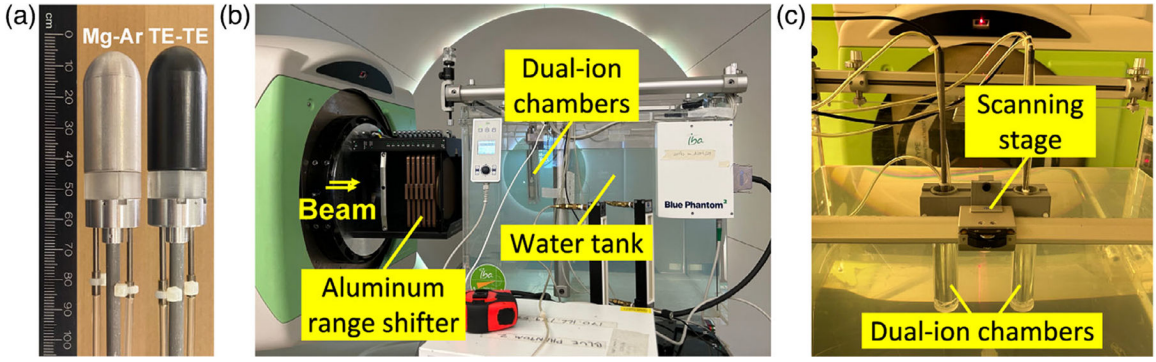

FIGURE 2.

(a) Pre-manufactured TE-TE and Mg-Ar ionization chambers. (b) Dual-ionization chamber measurement setup. (c) Ion chambers mounted onto the scanning stage of a water tank measuring (675 × 645 × 560) mm^3 and aligned along the central axis at 5 cm downstream from the Bragg Peak. TE-TE, tissue-equivalent wall filled with tissue-equivalent gas. Mg-Ar, magnesium wall filled with Argon gas.

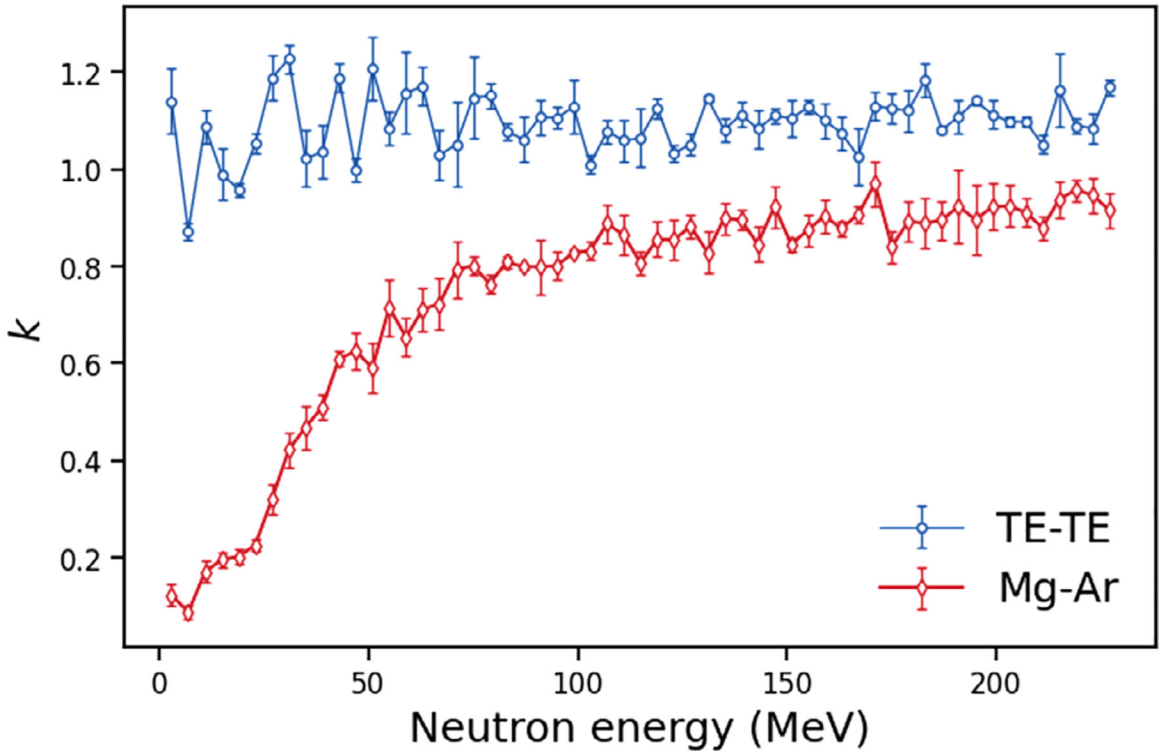

FIGURE 3.

Relative neutron sensitivity (*k*) simulated with TOPAS as a function of incident neutron energy for the TE-TE and Mg-Ar chambers. TE-TE, tissue-equivalent wall filled with tissue-equivalent gas. Mg-Ar, magnesium wall filled with Argon gas.

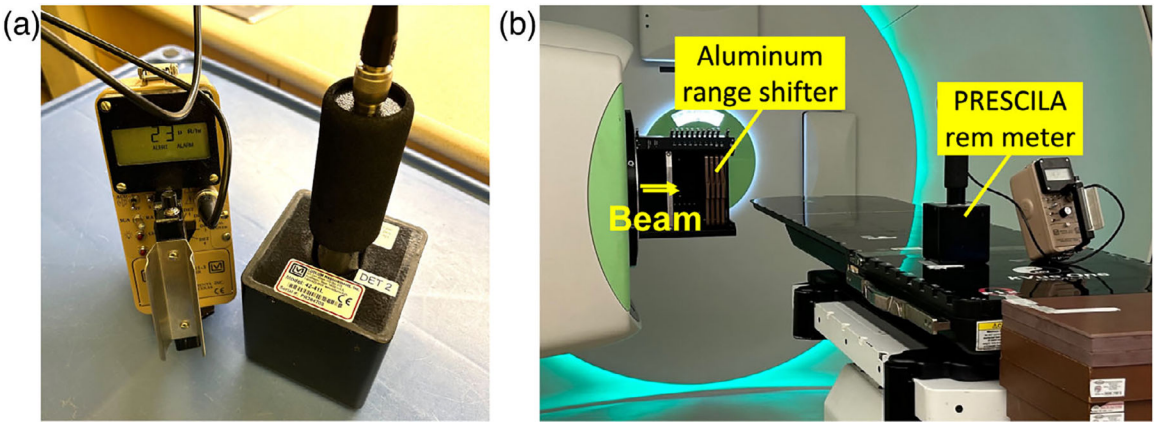

FIGURE 4.

(a) PRESCILA rem meter. (b) Far out-of-field secondary neutron measurement setup with the rem meter placed at 0.5 m from the central axis. PRESCILA, Proton Recoil Scintillator-Los Alamos.

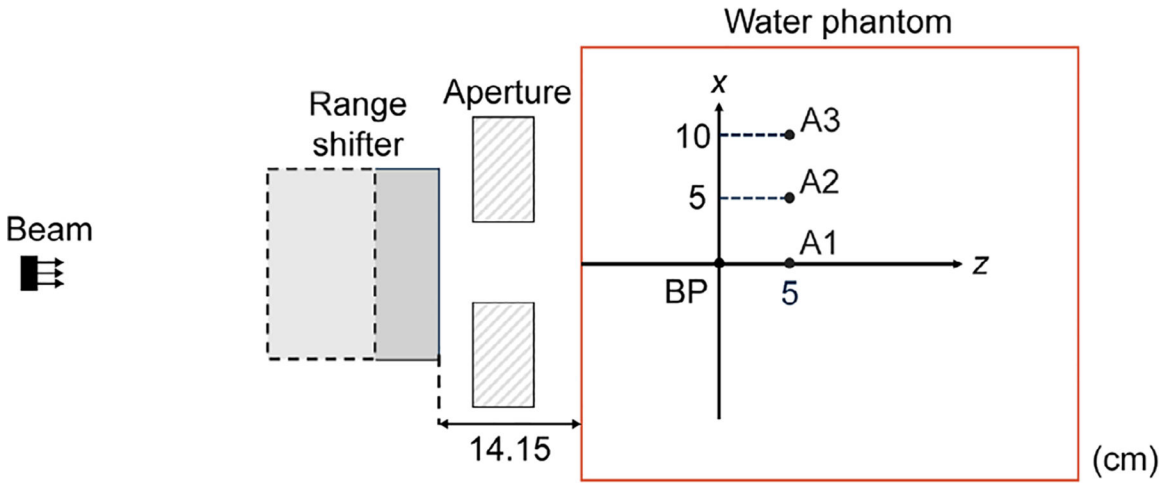

FIGURE 5.

Schematic (not to scale) of Monte Carlo simulation geometry including a proton source, a range shifter of various thicknesses, an aperture, a (30 × 30 × 40) cm^3 water phantom with isocenter defined at the Bragg peak (BP). Positions A1, A2, and A3 at a lateral distance of 5, 10, and 15 cm from the central axis and 5 cm downstream from the BP were used for validating with measurements. The area within the red square indicates the simulation scoring region.

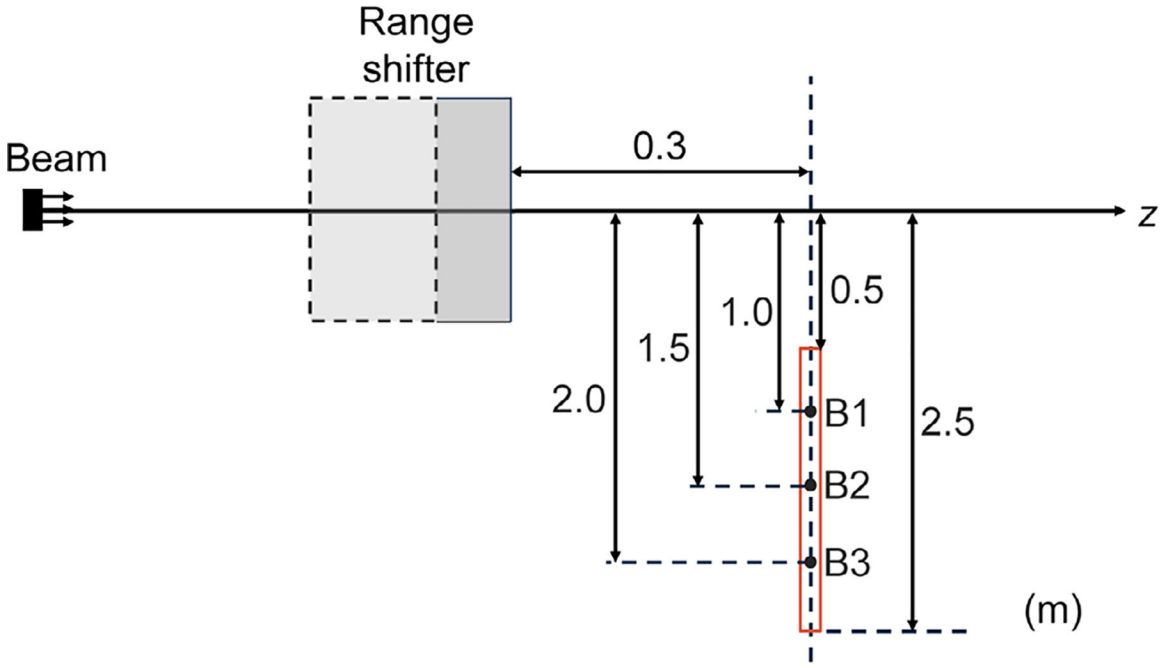

FIGURE 6.
Far out-of-field neutron dosimetry simulation setup (not to scale) with the red rectangle indicating the scoring area. B1, B2, and B3 at a distance of 1, 1.5, and 2 m from the central axis (*z*) indicate the measuring positions for simulation validation.

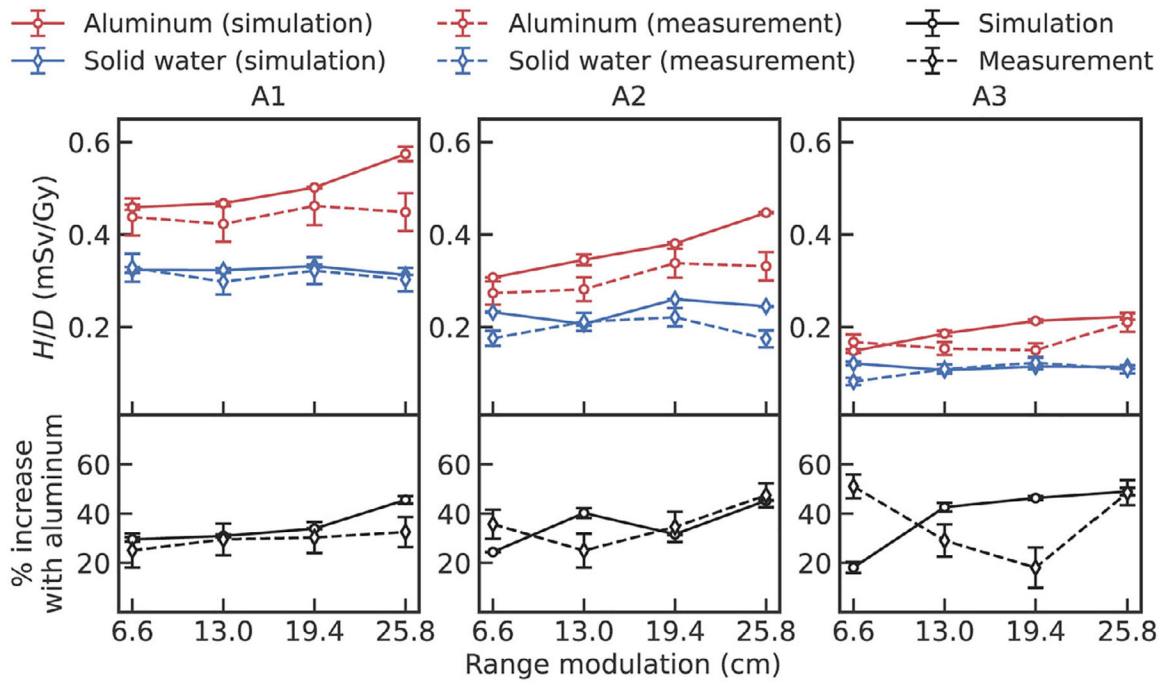

FIGURE 7.

Simulated and measured out-of-field secondary neutron dose equivalent per therapeutic dose at A1, A2, and A3 with range modulation using aluminum and solid water. The percentage increase in the values for the aluminum cases relative to the solid water cases is shown in the bottom row.

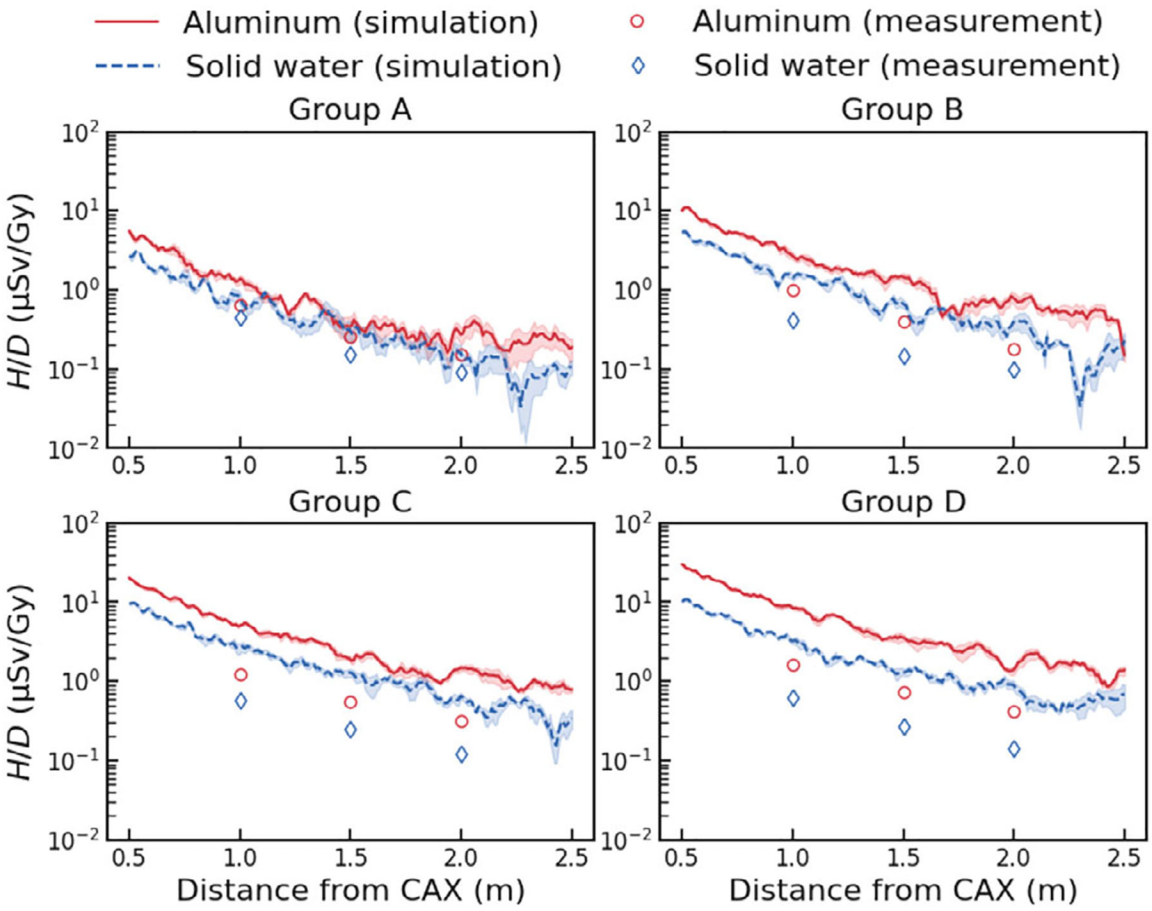

FIGURE 8.

Simulated dose equivalent per therapeutic dose of secondary neutrons at a lateral distance of 0.5 to 2.5 m from the CAX with measured values at B1, B2, and B3 using PRESCILA rem meter. The shaded region indicates the uncertainties for simulation results; uncertainties in measurement results are not shown as they are smaller than the marker size. CAX, central axis; PRESCILA, Proton Recoil Scintillator-Los Alamos.

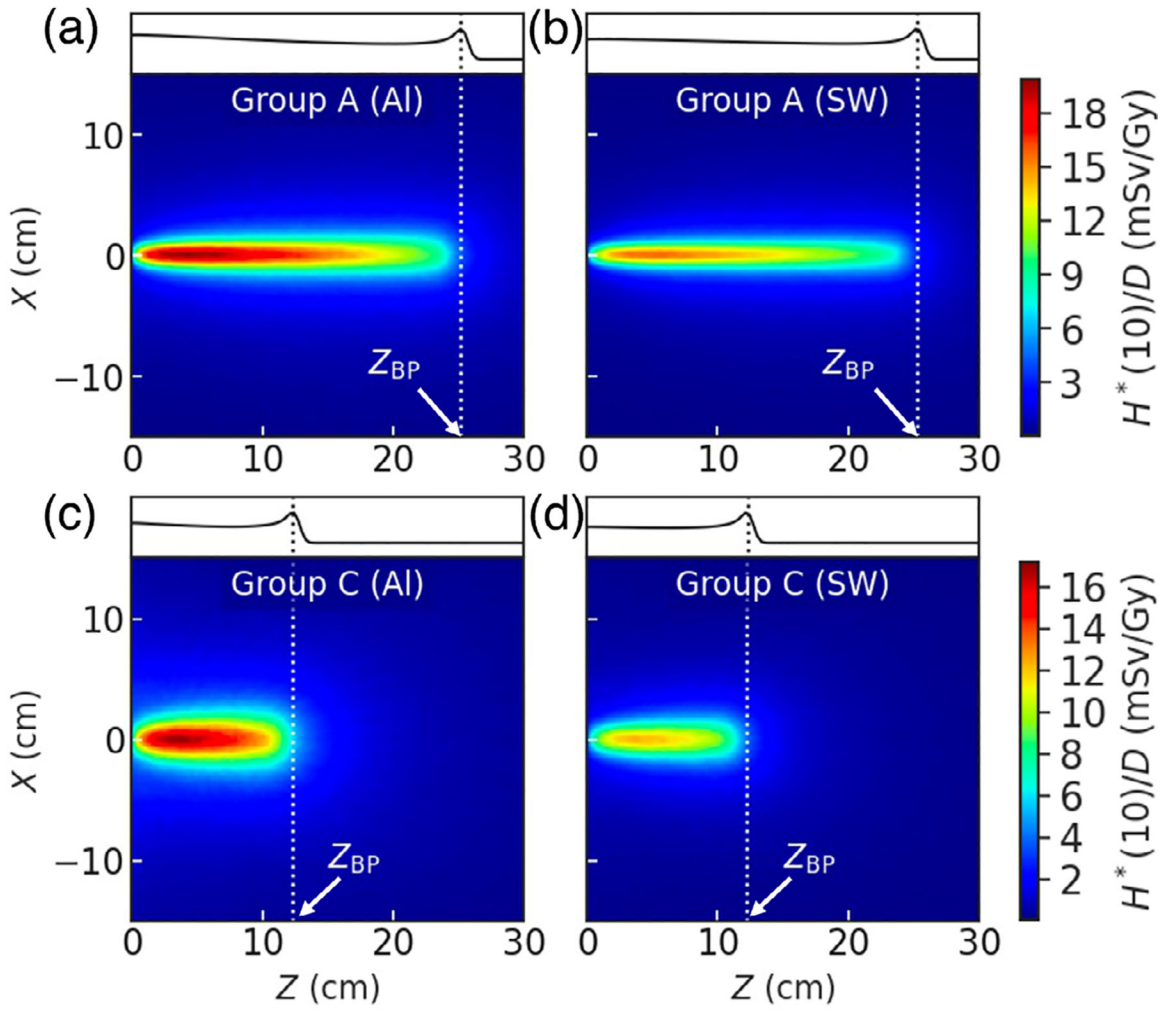

FIGURE 9.

Ambient neutron dose equivalent per therapeutic in the *xz*-plane with Al and SW range shifters modulated depths of the Bragg peak at Z_{BP} = 25.1 cm and Z_{BP} = 12.3 cm (dotted lines) for Group A (a, b) and Group C (c, d) respectively. Panels in the same row share the color bar in that row. Al, aluminum; SW, solid water.

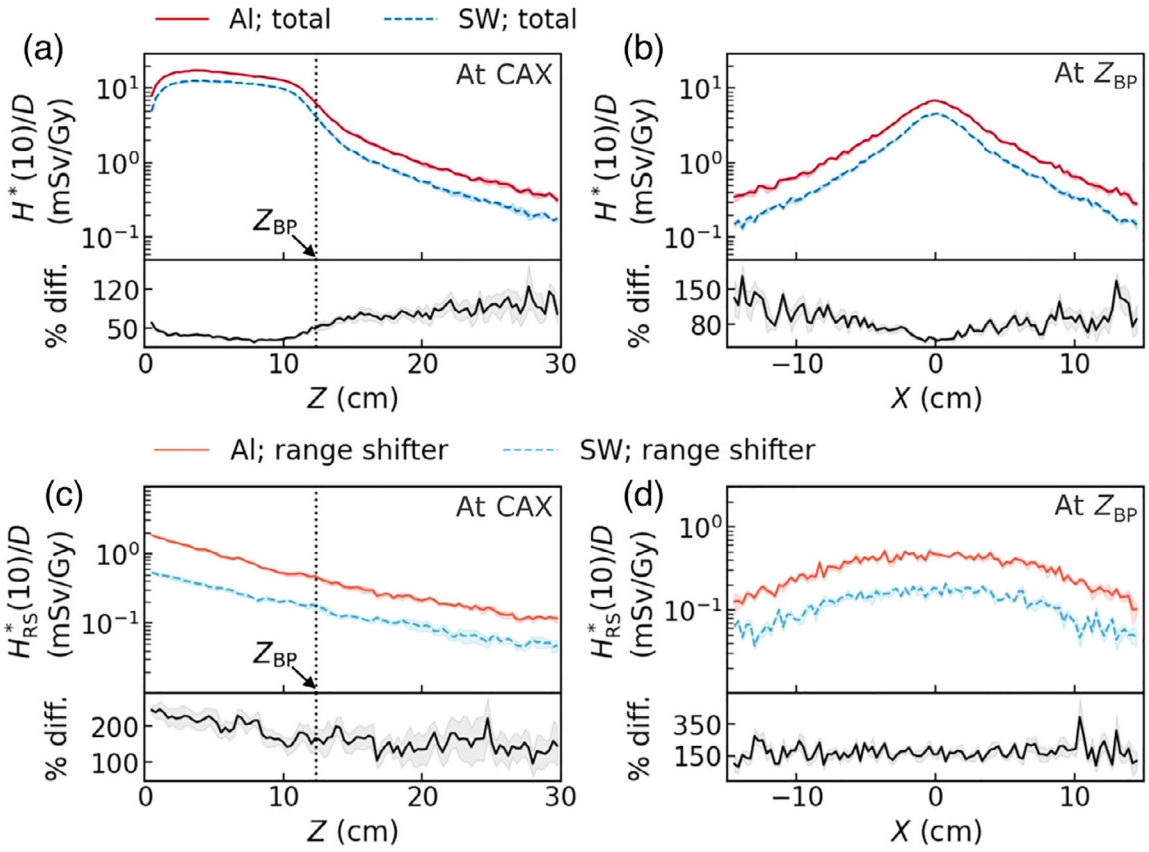

FIGURE 10.

Group C ambient neutron dose equivalent per therapeutic dose with standard errors (shaded region) for all the secondary neutrons ($H^*(10)/D$) (a, b) and the neutrons produced in the range shifter ($H^*_{RS}(10)/D$) (c, d) with percentage difference (% diff.) as a function of depth on the CAX and along the x-axis at the Bragg peak depth Z_{BP}=12.3 cm (dotted line) for Al and SW. Al, aluminum; CAX, central axis; SW, solid water.

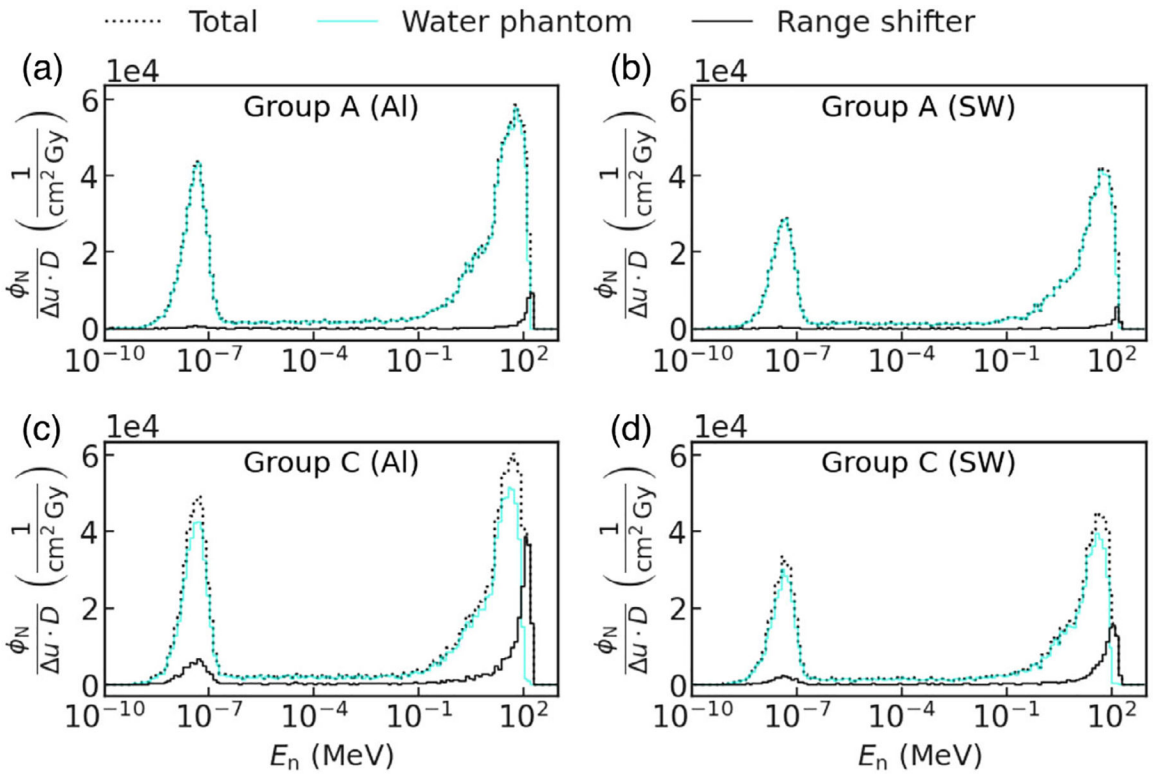

FIGURE 11.

Secondary neutron fluence spectra at A1 in lethargic unit per therapeutic dose and the spectrum components for the neutrons produced in either the water phantom or the range shifter for Group A with (a) 3-cm Al plates or (b) 6.4-cm SW slabs for a 6.6 cm of range modulation and Group C with (c) 9-cm Al or (d) 19.5-cm SW for a 19.4 cm of range modulation. Al, aluminum; SW, solid water.

TABLE 1

Aluminum and solid water range shifter (RS) thicknesses (t_{Al} and t_{SW}) with the corresponding range modulation (mod.) and the Bragg peak depth (Z_{BP}) in water for 225 MeV proton energy.

Group	t_{AI} (cm)	t_{sw} (cm)	Range mod. (cm)	Z_{bp} (cm)
A	3.0	6.4	6.6	25.1
B	6.0	12.9	13.0	18.7
C	9.0	19.5	19.4	12.3
D	12.0	25.9	25.8	5.9

TABLE 2

Range shifter material composition used in the simulations with percentage mass fraction for each element.

Material	Density (g/cm^3)	Element	Mass fraction (%)
Aluminum	2.7	Aluminum	100.0
Solid water	1.0	Carbon	67.2
		Oxygen	19.9
		Hydrogen	8.1
		Nitrogen	2.4
		Calcium	2.3
		Chlorine	0.1

TABLE 3

Summary of simulated and measured secondary neutron dose equivalent per therapeutic dose at a distance close to the irradiation field (5 cm downstream from BP and ≤15 cm laterally from beam axis) in the water and far out of the field in the air for a range modulation between 7 cm and 26 cm achieved by aluminum or solid water.

		H/D (μSv/Gy)	
Range shifter	**Method**	**≤15 cm**	**1–2 m**
Aluminum	Simulation	148(4)–570(20)	0.27(7)–8.8(5)
	Measurement	150(20)–460(40)	0.151(7)–1.62(2)
Solid water	Simulation	107(2)–324(6)	0.16(4)–3.3(3)
	Measurement	81(8)–330(30)	0.093(2)–0.63(3)

Note The digits in parentheses are the uncertainty.